Early-Stage Phase Separation in Polyimide Precursor Blends: An Atomic Force Microscopy Study

Ravi F. Saraf

T. J. Watson Research Center, IBM Corporation, Yorktown Heights, New York 10598

Received December 23, 1992; Revised Manuscript Received April 2, 1993

ABSTRACT: The surface of polyimide precursor blends is studied using atomic force microscopy (AFM). The acid (PAA) and ester (PAETE) precursors in the blends are of the same polyimide. The topographical contrast is due to the complexation of solvent with the acid precursor, causing the latter to swell. Early-stage phase separation prior to impingement is studied for a blend with 20% weight fraction of PAA relative to PAETE. The growth rate of the domains is by nucleation and growth. The PAA-rich discontinuous phase grows at a rate of $\sim t^1$ rather than the $t^{1.5}$, which is usually obtained for surface-induced phase separation. The study also demonstrates the effect of moisture on the acid precursor. It is further shown that due to ~15-fold faster kinetics of imidization of PAA relative to PAETE, the phase-separated topography is maintained even after both precursors convert to the same polyimide.

Introduction

Multicomponent polymer systems composed of incompatible components are of both technological and scientific importance. Materials such as high-impact polystyrene (HIPS) and poly(acrylonitrile–butadiene–styrene) (ABS) have found applications as important structural materials with a combination of rubbery and glassy properties.[1,2] Scientifically, polymer-based system, due to their slow dynamics, have become especially convenient to study phase separation behavior in binary fluids.[3–7] This area of active investigation utilizing techniques such as small-angle light scattering and neutron scattering has probed the growth process (and mechanism) in the bulk. Recently (and naturally), there has been great interest, motivated by theoretical predictions,[8–10] in experimentally studying the spinodal decomposition in the vicinity of an interface. Wiltzius and Cummings reported the dynamics of phase separation using SALS.[11] They found that the fast-growth mode (parallel to the surface) due to preferential wetting of one phase over the other scales as $t^{1.5}$. Guenoun et al. have studied the late-stage development, finding a scaling exponent of 1.[12] Using forward recoil spectroscopy, Jones et al. have observed that the static structure factor of the phase-separated system at deep quench oriented normal to the interface.[13] Their growth seems to scale as t^1. Bruder and Brenn have studied the effect of interface (air and substrate) on spinodal decomposition in polymer thin films.[14] In the present paper, we study the phase separation phenomena in polymer blends using AFM. Since AFM is sensitive to structure at the air/polymer interface, this method is especially suited to measure phase separation phenomena affected by interfacial forces (or energy). This study differs from the above in two respects: (i) the interface is air/polymer rather than a dense third phase (like glass); (ii) the instability in a one-phase system is achieved by evaporating solvent.

The polyimide precursor blends chosen for this study are of great technological importance in the microelectronics industry for chip packaging application and flex circuits due to their low dielectric constant, high temperature stability, and low thermal expansion coefficient.[15] Although high-temperature polyimides such as PMDA–ODA and BPDA–PDA are not soluble (except in concentrated sulfuric acid and the like[16]), the acid and ester precursor forms are easy to process and are soluble in polar solvents such as *N*-methylpyrrolidinone (NMP).[17] Furthermore, in recent years UV light sensitive polyimides, referred to as photosensitive polyimides, have been developed. These materials will significantly reduce the processing cost of constructing multilayer structures for chip packaging if successfully engineered.[18,19] The importance of polyimide is further augmented by its application as a matrix material in constructing high-performance composites in the aerospace industry.[20] Polyimide copolymers have also been constructed for application as structural adhesives in the aerospace and microelectronics industries.[21]

The length scales probed in the present study fall in the 10^1–10^3 nm range; this is complementary to techniques using visible light (such as light scattering and optical microscopy) and neutron (or X-ray) scattering. Furthermore, AFM is sensitive to observing changes in films with thicknesses <300 Å to >10 μm provided the surface remains relatively flat. This paper discusses the contrast mechanism to observe phase separation in a blend using AFM. Then the nucleation and growth phenomenon is described by observing the surface topography of the blend. We shall also briefly describe the image analysis program to quantify the growth process. It will become apparent in this report that AFM can be a useful tool in quantifying early phase separation behavior in polymer blend (and maybe crystallization) systems that allow ex-situ measurement. The technique is surface sensitive and applicable on ultrathin films.

Experimental Section

A blend of ethyl ester (PAETE) and acid (PAA) precursors of poly(pyromellitic dianhydride–oxydianiline) (PMDA–ODA) polyimide was prepared in *N*-methylpyrrolidinone (NMP) solvent. The weight fraction of PAA with respect to PAETE was kept constant at 0.2 for this study. The effect of composition on the morphology and phase separation will be reported in a separate paper. The three-component, one-phase blend was prepared in NMP with weight fraction $f < 94\%$ of the total polymer. The PAA and PAETE were supplied by DuPont as Parline 5878 and 5801 resins, respectively.

The ternary solution was spun on a single-crystal silicon wafer with ~30-Å native oxide. The thickness of the film was controlled by the spinning speed. The film thickness was measured by an α-step device made by Telcor. The thickness at several different areas was sampled to verify the planarity of the film. The reason for using a single-crystal silicon wafer is to ensure a smooth (roughness < 1 nm) and flat surface for the AFM studies. The sample was immediately placed in a dry-N_2-flushed oven con-

0024-9297/93/2226-3623$04.00/0

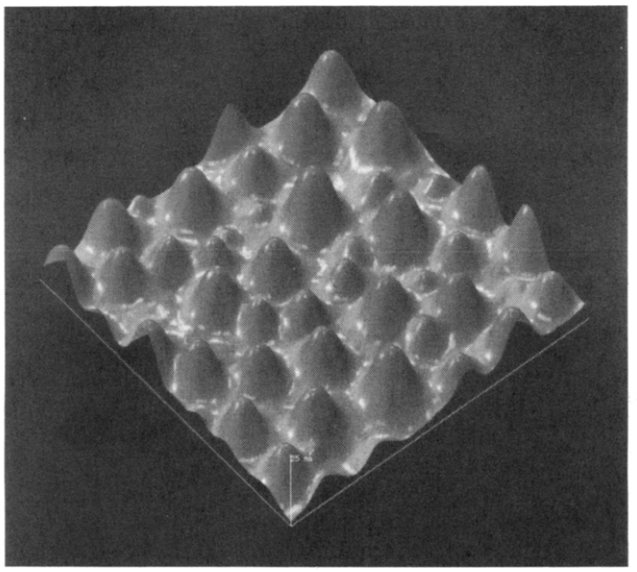

Figure 1. 4000 × 4000 nm AFM micrograph of PAA/PAETE 20/80 blend soft-baked at 70 °C. The final thickness of the film T_{SB} = 206 nm. The topographical contrast is due to compexation of NMP with PAA.

trolled at 70 °C to drive off the solvent. To avoid moisture absorption, which alters the surface morphology (as will be apparent in Figure 5), we conducted the experiment in a clean room with ~30% relative humidity. The soft-baked films were analyzed using AFM. The microscopy was performed immediately to avoid significant moisture uptake, and the samples were always stored in a desiccator under vacuum. Subsequently, the wafer was hard-baked to 400 °C in a preheated dry-N_2-flushed oven. To avoid heat loss and oxidation, the sample was placed in-situ in the oven. We note here that although such a fast annealing rate may not produce the optimum film properties, the purpose is to quench-in the morphology due to the phase separation process during the soft-bake process.

The AFM used to observe the surface topography is manufactured by Digital Instruments, Inc. The AFM was operated in a repulsive mode, and the deflection of the tip was measured using the shift in the reflected beam from the cantilever using a two-sector detector. Although the deformation of the sample due to the tip for the length scales of interest in this study was negligible, we tried to optimize the tip-to-sample contact force to the minimum possible value. For every sample, we gradually brought the tip close to increments of 100 nm to achieve contact forces in the 100–400-nN range. The scans were performed close to 100-nN contact force. By scanning the same area more than 50 times, it was ensured that the tip did not cause any permanent deformation. The invariance in the topography as the contact force was increased from 100 to 400 nm implies the elastic deformation is also negligible for the length scales measured in this study. We also note that the image distortion due to hysteresis in the piezoelectric motor is negligible in the x–y direction compared to the feature size measured. The data were analyzed using in-house image analysis programs. The images were produced using GALAXY on a IBM RISC-6000 system.

Results and Discussion

To differentiate phase-separated regions by AFM, it is essential to have significant differences in relative volumetric change to cause surface topographical features. Figure 1 shows a PAA/PAETE blend after soft-bake at 70 °C. As the solvent evaporates, the system phase separates into discontinuous PAA-rich regions in the PAETE-rich matrix. From density considerations, the PAA-rich region is expected to be more dense due to stronger intrachain interactions and smaller chain cross-section, leading to better packing in the amorphous phase. Furthermore, we observe that in a well-mixed blend with f = 85% solvent, the PAA-rich phase settles at the bottom. However, the

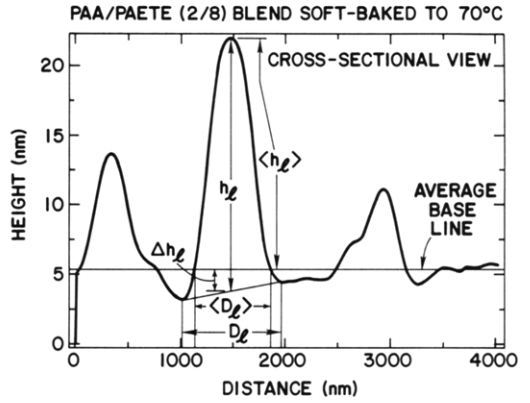

Figure 2. Cross-sectional view of Figure 1 through the large *hills*. The average base line at 5.11 nm calculated from the height histogram (see Figure 10) is higher than the base line apparent from the curve. This discrepancy results in lower average height $\langle h_l \rangle$ and diameter $\langle D_l \rangle$.

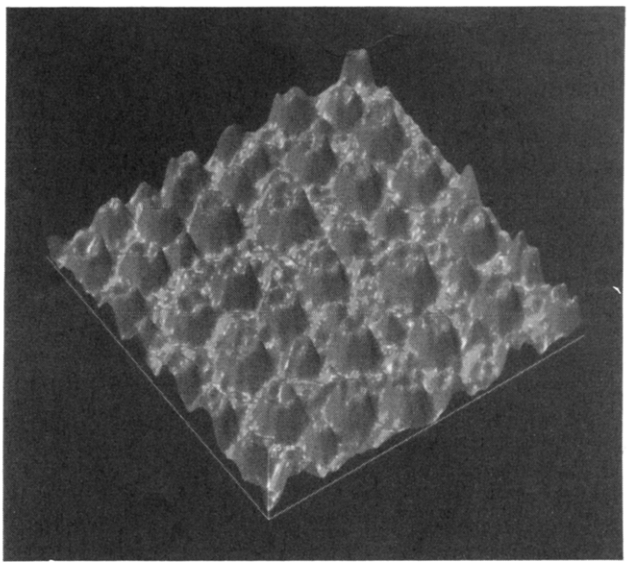

Figure 3. AFM micrograph of a sample similar to that of Figure 1 after hard-bake at 400 °C. The final thickness of the sample T_{HB} = 119 nm. Although both PAA and PAETE imidize to the same polymer, PMDA–ODA, the phase-separated morphology persists due to the relatively faster rate of imidization of PAA compared to that of PAETE. For comparison, the scale in the x–y plane and the z direction is the same as that in Figure 1.

discontinuous PAA-rich regions are elevated rather than depressed as is evident in Figure 1. The reversal in surface topography is attributed to swelling caused by ~20% of complexed NMP (on an average of 1 NMP molecule per monomer unit) with PAA that is not liberated during the soft-bake.[22] Since the complexation is due to hydrogen bonding, no swelling of PAETE occurs. Consequently, the PAA-rich regions are swollen more relative to the PAETE-rich matrix. Figure 2 shows a cross-sectional view through one of the large *hills*. By taking several cross-sectional views, the lateral size (D_l) and height (h_l) of the largest phase-separated regions are measured to be 750 ± 50 and 15.5 ± 1.5 nm, respectively. For reasons discussed later, in this paper we shall subsequently characterize the topography by their large-size features.

Figure 3 shows the surface topography after the sample of Figure 1 is hard-baked at 400 °C. Although both PAA and PAETE imidize to PMDA–ODA, the phase-separated morphology is maintained. Retention of phase-separated morphology may be explained by analyzing the kinetics of imidization during the hard-bake process. The activation energy ΔE for imidization of PAA is ~25 kcal/

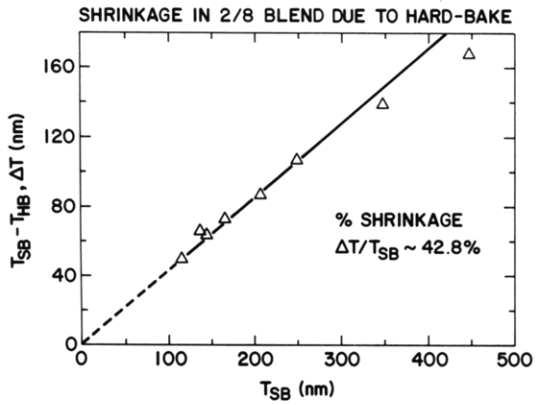

Figure 4. Change in thickness from soft- to hard-baked ($T_{SB} - T_{HB}$) versus T_{SB} indicates a constant shrinkage of 42.8%. The deviation from linearity at larger thickness is attributed to solvent entrapment caused by faster evaporation at the surface.

mol.[17] Although the ΔE for PAETE is higher than that for PAA, as an approximation, we assume equal activation energy. Since the threshold temperature of PAA and PAETE is 140 and 180 °C, respectively,[23] the rate of imidization (and the first-order rate constant, k) in former is ~15-fold faster than in the latter. Since ΔE is (assumed to be) the same for the PAA and PAETE, the ratio of the two rate constants remains constant over all temperatures. Typically, for PAA > 80% imidization occurs in 45 min at 150 °C.[24] Since percent conversion is $\sim(1 - e^{kt})$ and $k \sim e^{-\Delta E/k_B T}$, the time for 80% imidization at 200 °C for PAA is ~1.7 min. In contrast, the imidization for PAETE at 200 °C would take ~25 min. We installed a thermocouple in the sample holder to measure the sample temperature. The sample reached 200 °C in ~2.5 min. Thus, ~80% imidization of PAA is complete by the time the sample has reached 200 °C. Assuming a 15-fold lower k, ~5% of PAETE will be imidized by the same time. Therefore, it is reasonable to assume that during the imidization of PAA to polyimide PI1 (liberating the complexed NMP) phase-separated *hard-balls* are formed while the PAETE is essentially unimidized. We note that the kinetics of imidization of PAA is faster than that of PAETE by an amount larger than predicted above, due to the mobility (induced by complexed solvent in PAA) and the higher ΔE for PAETE. Subsequently, when the matrix PAETE imdizes to polyimide PI2, the PI1 *hard-balls* are pushed upward due to the shrinkage caused by imidization of PAETE, resulting in *hills* remaining intact. It is noted that although PI1 and PI2 are both PMDA–ODA, we differentiate them for clarity in the discussion. The (mutual) diffusion of PI2 (as it forms) in PI1 is prohibitively slow because the T_g of PMDA–ODA, >400 °C, is well above the curing temperature.

Comparing the surface topography of Figures 1 and 3 indicates that the height of the large *hills* h_1 reduces from 15.5 ± 1.5 to 8 ± 1 nm. The shrinkage is due to the release of complexed NMP during hard-bake and the rise in density caused by imidization from an amorphous to a partially ordered structure. The relative change in the total film thickness due to hard-bake, $(T_{SB} - T_{HB})/T_{SB}$ (T_{SB} and T_{HB} are thicknesses after soft-bake and hard-bake), is ~42.8% as calculated from the slope in Figure 4. The 5.2% change in the shrinkage of *hills* compared to the total film thickness is attributed to the complexed solvent in PAA and the larger increase in density of PAETE relative to PAA on imidization. We note that the above-mentioned reasons for differential shrinkages will tend to compensate each other. Due to this differential shrinkage, the PI2 matrix in the bulk is in slight tension and the embedded PI1 *hard–balls* are in slight compression. The existence of stress transfer indicates good adhesion between the PI1 and PI2 regions. Furthermore, PI1 domains shrink concomitantly in the lateral direction by ~13% as evident by reduction in D_1 from 750 ± 50 to 650 ± 50 nm. This reduction in lateral direction is also attributed to evaporation of complexed solvent during curing.

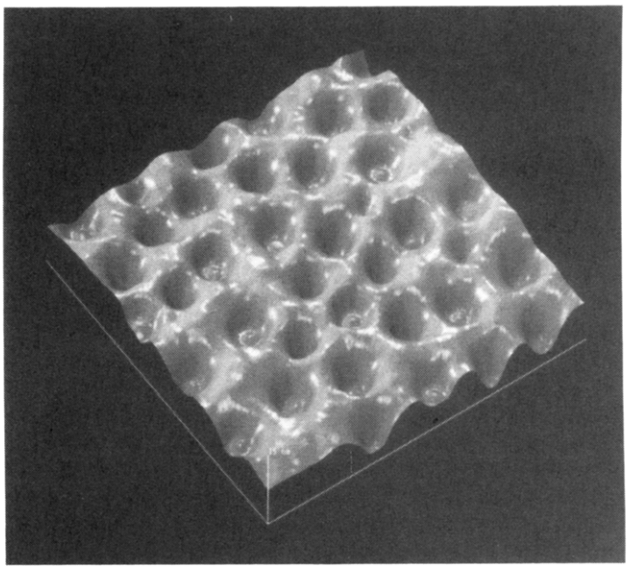

Figure 5. 4000 × 4000 nm AFM image of T_{SB} = 198 nm film soft-baked and then exposed to 100% relative humidity conditions at the same temperature. Due to the presence of moisture, the *hills* convert to *holes*.

From a structural standpoint and ignoring the kinetics of imidization, the expected contrast between PI1 and PI2 should basically arise due to a change in respective densities from their precursor states. This difference due to similarities in structures will be significantly smaller compared to the measured topography in Figure 3. Furthermore, the mutual diffusion during the imidization should also smear the topography. Thus, the persistence of phase-separated morphology in Figure 3 similar to Figure 1 clearly indicates the cascaded imidization process of PAA and PAETE discussed above. The persistence of morphology after hard-bake, in general, indicates that finite volumetric change may not be necessary to create a topographical contrast. The contrast can be created by controlling the kinetics.

The existence of an upward thrust due to the shrinking of the PAETE matrix on curing to PI2 is more dramatically seen in Figures 5 and 6. Figure 5 shows the PAA/PAETE blend after soft-bake at 70 °C followed by exposure to 100% relative humidity at the same temperature. Since, NMP has more affinity for water than PAA, the moisture leaches out the (complexed) NMP from PAA. Consequently, PAA shrinks, forming *holes* rather than *hills*. Evidence of the depressed *hills* is manifested as a small "dimple" seen at the center of some of the *holes*. We shall not pursue this point in this report but mention that this dramatic change in topography may be used to quantify the effect of moisture on the structure of polyimide films. To avoid complications due to moisture absorption, we processed our films under dry N_2. However, on imidizing such a film to 400 °C, the *holes* convert to *hills* as seen in Figure 6. This can be explained as follows: imidization of PAA to PI1 forms *hard-balls*; as PAETE → PI2, the *hard-balls* are pushed upward, forming *hills*. The height of the domains increases from ~−5 to ~+8 nm. We also note that the heights of *hills* in Figure 6 (formed from *holes*) and Figure 3 (formed from *hills*) are 8 ± 1.5 and 8 ± 1 nm,

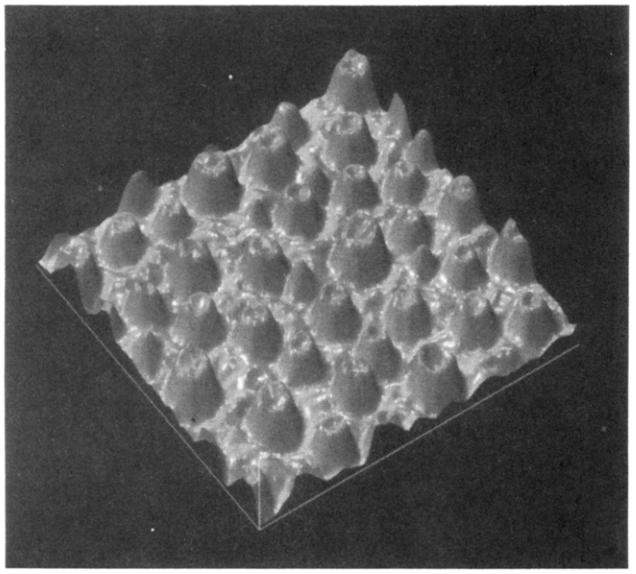

Figure 6. AFM image of a film identical to that in Figure 5 after a hard-bake to 400 °C. The final thickness T_{HB} = 119 nm is similar to the thickness of the film in Figure 3 with comparable surface topography. Note the scales of Figures 6 and 3 are identical.

respectively. The comparable height of the *hills* and reversal of contrast from *hills* → *holes* indicate that the morphology after 400 °C is principally due to the upward thrust exerted on the *hard-balls* during the PAETE curing process. The conversion of the morphology from *hills* to *holes* further proves the cascaded imidization of PAA followed by PAETE.

The size of the PI1 domains, i.e., the lateral dimension of the *hills*, is determined by the phase separation kinetics during the soft-bake process. Since the T_g of PAA and PAETE are nominally in the range 150–170 °C, the phase separation occurs before all the (uncomplexed) NMP evaporates during the soft-bake process. Thus, the solvent evaporation time τ determines the lateral size D_h of the *hills*. This is evident by comparing Figures 3 and 6, where the soft-bake conditions of two samples are significantly different, but the phase separation time τ is the same, resulting in a similar lateral dimension after hard-bake.

Figure 7 shows AFM micrographs of a blend spun at different speeds. The decrease in D_l is due to a decrease in τ caused by a decrease in T_{SB}. Comparing Figure 7a–c, we note that for τ = 61 s, corresponding to T_{SB} = 347 nm, impingement is observed (Figure 7a). For τ = 33 and 18 s, no impingement is observed. Figure 8 shows a monotonic increase in the lateral dimension with increasing τ. For films with τ < 45 s, corresponding to T_{SB} = 248 nm, the growth is linear. For larger τ the growth rate abruptly decreases. This slowing down in the growth rate is attributed to depletion of PAA concentration in the surrounding matrix as the domains grow closer to each other. The small decrease in nucleation density shown in Table I between τ = 45 and 61 s indicates that some coalescence may initiate at $\tau \sim 52$ s, corresponding to $T_{SB} \sim 280$ nm (from Figure 4). We note that the micrographs in Figure 7 are consistent with the value for the coalescence threshold. The rapid increase in D_l past the impingement threshold is prohibited due to an overlap of the depleted regions of phase-separated PI1. Later in this section we shall discuss the linear growth observed.

The invariance in the surface density of the features for film thicknesses corresponding to $\tau \leq 45$ s suggests that nucleation is heterogeneous. This implies that the vari-

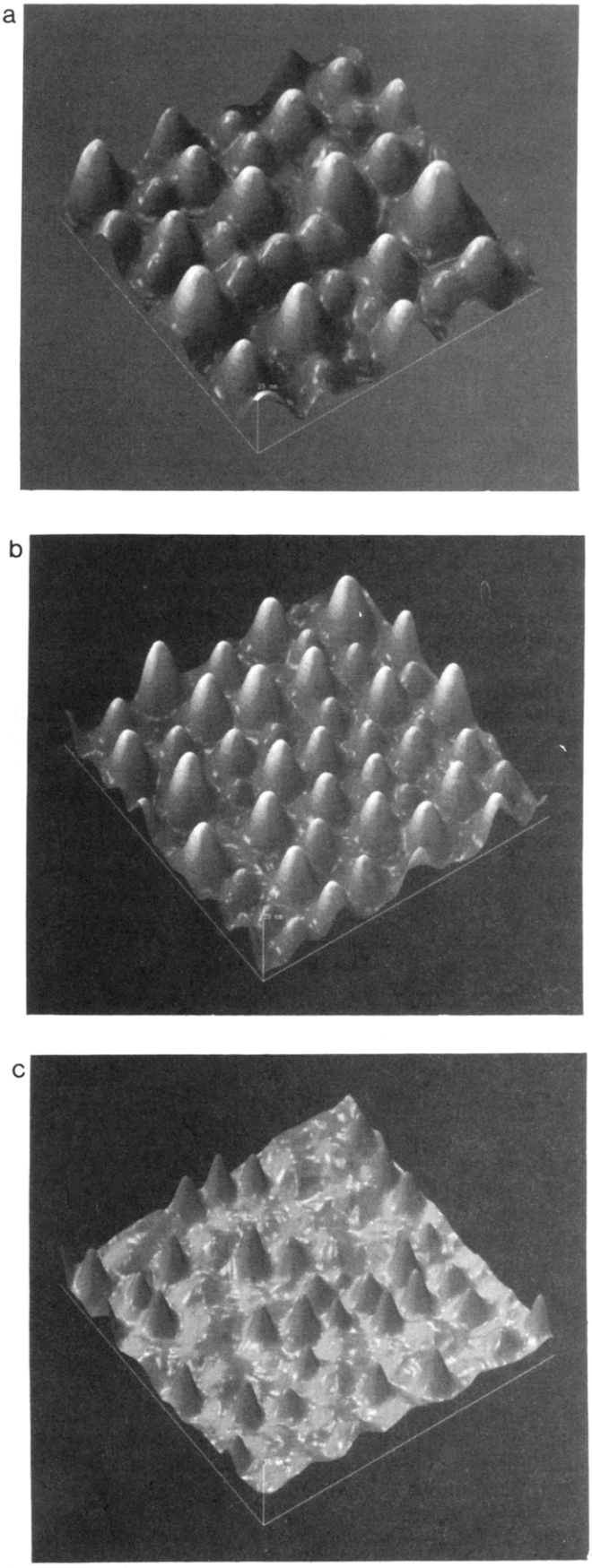

Figure 7. 4000 × 4000 nm AFM image of PAA/PAETE 20/80 blend at T_{SB} and τ of (a) 347 nm and 61 s, (b) 165 nm and 33 s, and (c) 115 nm and 18 s. The difference in the lateral dimension and height decreases as the evaporation time τ, proportional to growth time, decreases. The impingement in the thicker film leading to a lower nucleation density is apparent in the thickest film.

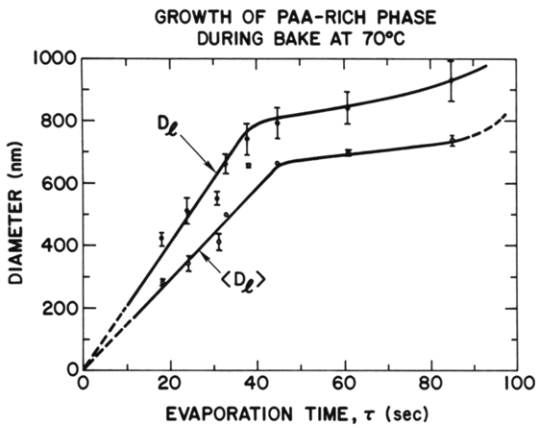

Figure 8. Lateral diameter of the large *hills* measured manually from cross-sections (D_l) and from the height histogram (Figure 10) ($\langle D_l \rangle$) increases linearly with evaporation time τ prior to impingement. $D_l > \langle D_l \rangle$ is consistent with Figure 2.

Table I. Phase Separation in PAA/PAETE 20/80 Precursor Blend

thickness T_{SB} (nm)	height h_i (nm)	nucleation density (#/10^3 nm^2)	fraction of large *hills* (%)
447	17.6 ± 1.6	9.0	14
347	19.5 ± 1.5	9.50	13
248	17.0 ± 1.0	11.00	18
206	15.5 ± 1.5	11.75	21
165	14.5 ± 0.7	12.00	15
144	8.5 ± 0.5	12.25	17
136	7.5 ± 0.4	12.38	29
115	6.3 ± 0.5	12.13	30

ation in size distribution is due to the proximity of the *hard-balls* to the surface. To estimate the effect of τ on D_h, we consider only the largest D_h which corresponds to growth during a time lapse of τ. The largest D_h designated as D_l, corresponds to >13% of the total number of *hills* observed (see Table I).

The total time of the soft-bake process does not have a significant effect on D_h. Parts a and b of Figure 9 show AFM micrographs corresponding to hard-baked PMDA–ODA films that were soft-baked at 80 °C for 5 and 120 min, respectively. The D_l for the 120-min baked film is ~40 nm larger than that for the 5-min baked film, signifying growth during the soft-bake after the evaporation of uncomplexed NMP. Since 40 nm lies well within the error margin of AFM measurement, no significant growth occurs after the evaporation of uncomplexed NMP. This postgrowth period after the evaporation of complexed solvent is not pursued in this study; however, it is minimized by annealing the sample for 2–3 min past τ.

Before discussing the linear growth rate in Figure 8, we describe the method to obtain the average lateral dimension $\langle D_l \rangle$ for the large *hills* from the AFM micrograph. Figure 10 shows the height distribution function $f(h)$ for the surface topography shown in Figures 1 and 3. As mentioned above, the size (height and diameter) of the large *hills* is an important parameter to develop a quantitative understanding of the separation kinetics. The maxima in $f(h)$ occur at h_l = 5.11 and 4.90 nm for the soft-baked and hard-baked samples, respectively, are the heights that occur most often, and thus are assumed to be the nominal base lines for the two surfaces. The invariance in the shape and location of the histogram peak indicates that the surface topography of the matrix does not change significantly upon hard-bake, indirectly implying that the solvent evaporation and curing process leaves the surface roughness unaffected except for the topography due to phase separation. The abrupt change in population

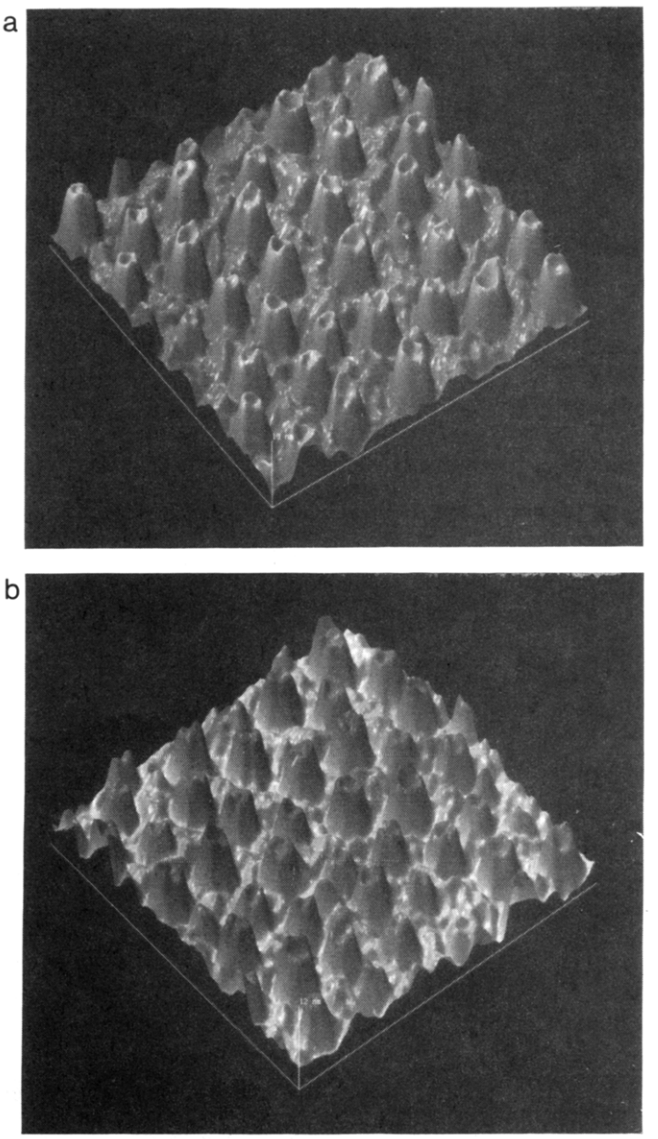

Figure 9. 4000 × 4000 nm AFM image of a blend soft-baked at 80 °C for (a) 5 and (b) 120 min. The *hills* in the latter image are nominally larger by ~40 nm in the lateral direction, indicating no significant growth after the solvent is evaporated.

density at 17.5 and 12.5 nm for the soft- and hard-baked samples corresponds to the average height of the large *hills* from the arbitrary zero. The average height from the nominal base line, $\langle h_l \rangle$, is 12.39 and 7.60 nm, respectively. We note that the average shrinkage of ~39% is more consistent with the overall shrinkage of 43% as shown in Figure 4, implying lesser strain than predicted above. That h_l obtained from a cross-section is larger than $\langle h_l \rangle$ measured from the histogram is evident in Figure 2. The latter is shorter because the nominal base-line is higher by Δh_l.

To compute the average size of the large PAA-rich domains, we section the image at the nominal base line and calculate the total area of the largest domains. Assuming circular geometry, the average size, $\langle D_l \rangle$, is determined from the measured area. As is evident from the cross-section in Figure 2, most of the clusters seem agglomerated except for a few individual features. The statistics is improved by sectioning images taken from random areas of the sample. The large clusters correspond to $\langle D_l \rangle$ = 665 ± 5 nm. Thus, the average size $\langle D_l \rangle$ and $\langle h_l \rangle$ are objective parameers to quantify the growth process and describe the relative change in topography. Similar to height, $\langle D_l \rangle < D_l$ as is evident in Figure 2. Figure 8

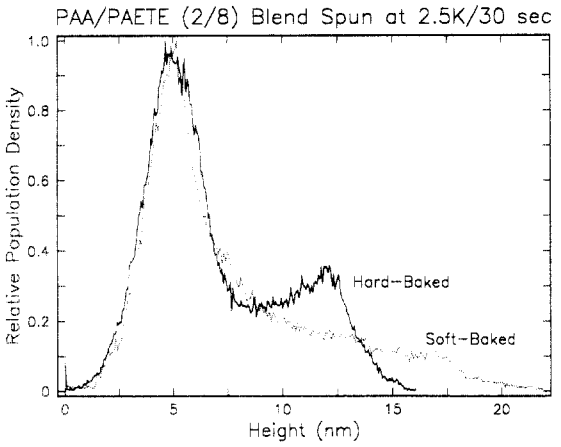

Figure 10. Relative fractions of various heights sampled in images in Figure 1 (soft-bake) and Figure 3 (hard-bake) indicate insignificant shift in the base line located at the maxima. The average height $\langle h_1 \rangle$, however, shrinks from 17.5 to 12.5 nm. The invariance in the shape of the base line peak also indicates that the hard-bake does not change the surface topography of the matrix (which is nominally pure PAETE) significantly.

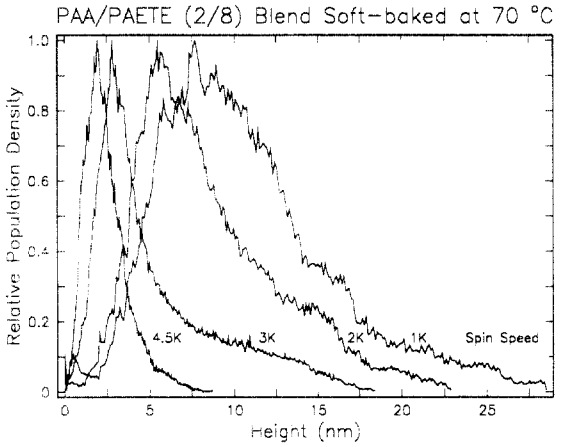

Figure 11. The base line peak broadens with evaporation time, corresponding to thicker films. Since $h_1 = 0$ is arbitar, the broadening shifts the height of the base line to larger distances with τ. The curves indicate more structure for thicker films due to a broader size distribution caused by impingement.

shows both D_1 and $\langle D_1 \rangle$ as a function of τ. The transition from linear region growth rate to the onset of impingement is more prominent in $\langle D_1 \rangle$ vs τ than D_1 vs τ. This partially justifies the relevance of an average size $\langle D_1 \rangle$ over the manually measured size, D_1.

Figure 11 shows a typical height histogram obtained for four films with different T_{SB}'s. It is quite evident that the maximum height h_1 increases from 6.74 to 19.64 nm as the evaporation time τ increases from 18 to 85 s. This is consistent with the growth of PAA-rich *hills* with longer τ. Furthermore, in the thicker films, the height histogram $f(h)$ decreases gradually with multiple local maxima. The latter corresponds to a broader distribution in the size of the *hills* due to impingement phenomena. Another consequence of the size distribution is a monotonic increase in the base line peak. The shift is attributed to increases in the width of the histogram peak, which in turn moves the location of the base line to higher height with respect to (arbitrary) zero.

Now we discuss the linear growth region observed in Figure 8 and mentioned earlier in the discussion. An important consideration in interpreting the growth process is to determine if there are any artifacts due to variations in the shape of the solvent concentration profile for thick versus thin films. For example, in thick films, if a dry skin

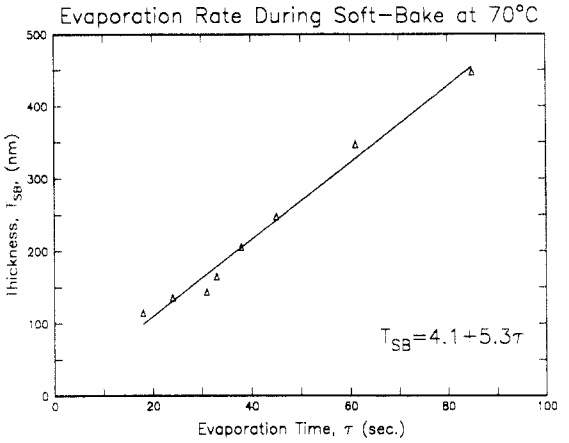

Figure 12. T_{SB} increases linearly with evaporation time τ, indicating that the rate of evaporation is constant for all thicknesses T_{SB}. Thus the solvent fraction in the film during drying versus $t/\tau(T_{SB})$, where t is time during the soft-baking process, is independent of T_{SB}.

is formed, it will enhance the rate of phase separation due to trapped solvent. On the other hand, if the thinner films are thin enough, the concentration profile of the solvent will show a gradual increase as a function of depth with no enhancement in growth rate due to trapped solvent. Figure 12 indicates that the drying time τ as a function of thickness is a linear function. The film thickness is measured by an α-step device. The intercept at 4.1 nm is within the resolution of the measurement, implying the line in Figure 12 passes through the origin. The linearity and the 0-nm intercept indicate that the concentration profile does change significantly as the film thickness increases; i.e., no skin formation occurs.

Next we calculate the solvent concentration ϕ as a function of depth. Since the functionality for drying time τ versus film thickness T_{SB} remains linear, we assume the effect of solvent concentration on solvent diffusion constant D is negligible. Conversely, if D changed with ϕ significantly, the thicker film would dry at a slower rate, implying nonlinear effects as the thickness increases. Similar to other flexible polymers, the diffusion constant D for uncured polyimide is $\sim 10^{-8}$–10^{-6} cm^2/s.[25] Thus the diffusion length in 1 s is $(4Dt)^{1/2} \sim 10^3$–10^4 nm $\gg T_{SB}$. Thus the rate of change in concentration profile is much faster than the shrinkage in film thickness L due to evaporation (i.e., quasi-static assumption). Using the above two assumptions and appropriate boundary and initial conditions (given in eqs i and ii of Appendix 1), the solvent concentration profile is given by eq iv in Appendix 1. The functionality of the profile is given by

$$\phi(z,t) = (\phi_1 - \phi_0)\,\phi\left(\frac{z}{L}, \frac{t}{L^2/4D}\right) \qquad (1)$$

The z/L functionality indicates that the profiles are self-similar and therefore are superimposable by scaling the z by the thickness L. The time dependence, given by $t^* = t/(L^2/4D)$, indicates that the rate of change in the profile with time is modified by $L^2/4D$; i.e., the profile changes at a *slower* rate for thicker films. Thus, the thickness controls the drying process in a self-similar manner in both space and time.

The independence of instantaneous thickness on the solvent concentration profile implies that the phase separation kinetics in all the films are subjected to comparable conditions during the drying process. The linear growth law of τ^1 will not be affected by variation in the solvent concentration as long as the initial concentration ϕ_0 of the solvent is kept constant. The change in

ϕ_0 will delay the time before the film begins to phase separate, shifting the $\langle D_l \rangle$ versus τ curve in Figure 8 along the τ axis.[26] As mentioned earlier, other studies predict an exponent of 1.5, in contrast to 1 found in this report.[12] Such a critical slowing-down in this system may be attributed to a shallow quench that may change the exponent from 1.5 to 1.[27] This may occur when the system freezes at a solvent concentration just below the binodal curve. As a result the phase separation will not proceed during the evaporation of the rest of the solvent. Other possible considerations may be complex hydrodynamic effects due to solvent evaporation, effects due to enrichment of the surface by PAETE, and effects of quench rate in the unstable region that are proportional to the drying rates. Nevertheless, it seems that the τ^1 scaling law is fundamental to phase separation growth rate due to evaporation of solvent in ternary polymer systems.

Conclusion

Early-stage phase separation in thin films of PAA/PAETE blend (with 2/8 relative weight ratio) was studied by AFM. The films' thicknesses ranged from 65 to 500 nm. The dimension of the PAA-rich discrete phase was in the 100–1000 nm range. Due to the PAA and NMP complexation, the discrete PAA-rich region was swollen relative to the PAETE-rich matrix. This topography was probed by AFM to observe the phase separation phenomena. The presence of complexed NMP was proven by exposing the film to moisture that leaches the complexed solvent out of the PAA-rich regions. Consequently, the elevated PAA-rich *hills* convert to *holes* (see Figures 3 and 6).

By regulating the film thickness, the time τ for solvent evaporation was controlled. Since the phase separation occurred only in the presence of the solvent, the growth of the PAA-rich region as a function of τ could be studied ex situ. A linear growth of the PAA-rich region was observed. The t^1 scaling law seems fundamental to such ternary systems. Impingement at longer evaporation times was observed by AFM (Figure 7a). A retardation in the growth rate occurred due to depletion of PAA in the matrix arising from close proximity of the regions. The evaporation time and thickness (for particular solvent concentration $f = 0.94$) at the onset of impingement phenomena were 52 s and 280 nm, respectively.

Acknowledgment. I would like to thank Drs. Daniel E. Platt and Clifford A. Pickover for their help in the production and analysis of the AFM images. I also thank Dr. Carlos J. Sambucetti for constant encouragement during this project.

Appendix 1: Solvent Concentration Profile during Drying of Thin Polymer Film

Let ϕ be the solvent concentration as a function of depth z. If we assume no concentration dependence on the diffusion constant D, the concentration profile is obtained by solving the equation

$$\frac{\partial \phi}{\partial t} = D\frac{\partial^2 \phi}{\partial z^2} \qquad \text{(i)}$$

The initial concentration of the solvent is ϕ_0. The drying process is initiated at $t = 0$ with an instantaneous drop in the surface concentration to ϕ_1 followed by diffusion of solvent from the bulk to the surface. Thus the boundary and initial conditions of the diffusion equation (i) are given by

$$\phi = \phi_0 \quad \text{at } t = 0 \text{ and } 0 \le z \ge L$$

$$\phi = \phi_1 \quad \text{at } t > 0 \text{ and } z = L \qquad \text{(ii)}$$

Since no solvent diffuses from the substrate side

$$\partial\phi/\partial z = 0 \quad \text{at } z = L \qquad \text{(iii)}$$

The problem is a moving-boundary problem because as the solvent evaporates, the thickness L changes. However, we make a quasi-static assumption by solving the diffusion equation (i) for constant L. Then we allow L to change with t in the final solution.

By taking the Laplace transform of the diffusion equation, the initial condition, and the boundary condition, the equation is solved exactly. The concentration profile is then calculated by Laplace inverse transform of the above solution.[28] The concentration profile obtained is given by

$$\frac{\phi(z,t) - \phi_0}{\phi_1 - \phi_0} = 1 + \frac{4}{\pi}\sum_{n=1}^{\infty}\frac{(-1)^n}{2n-1}\exp\left[-(2n-1)^2\left(\frac{\pi}{4\beta}\right)^2\right] \times \cos\left(\frac{(2n-1)\pi}{2}\frac{z}{L}\right) \qquad \text{(iv)}$$

where $\beta = L/(4Dt)^{1/2}$. The corresponding rate of evaporation N at (fixed) thickness L is given by

$$N = \left[D\frac{\partial \phi}{\partial z}\right]_{z=L} = -\frac{2D}{L}(\phi_1 - \phi_0)\sum_{n=1}^{\infty}\exp\left[-(2n-1)^2 \times \left(\frac{\pi}{4\beta}\right)^2\right] \qquad \text{(v)}$$

By the Poisson summation formula[28]

$$N = \frac{-4D\beta}{\pi L}(\phi_1 - \phi_0)\sum_{n=1}^{\infty}\exp[-4n^2\beta^2] \qquad \text{(vi)}$$

Typically, for uncured polymer $D \sim 10^{-8}$ cm^2/s is a reasonable upper limit.[25] The thickness of the films is $L \sim 10^{-5}$ cm. Thus, for the thin films studied that dry in $t \sim 10^1$ s, $\beta \sim 10^{-2}$. The small value of β indicates that the penetration depth for solvent evaporation is achieved within seconds. For small values of β eq v leads to

$$N \sim (\phi_0 - \phi_1)\frac{2}{\pi}\frac{D^{1/2}}{t} \qquad \text{(vii)}$$

References and Notes

(1) Bucknall, C. B. *Toughened Plastics*; Applied Science: London, 1977.
(2) *Rubber Modified Thermoset Resins*; Riew, C. K., Gillham, J. K., Eds.; Advances in Chemistry 208; American Chemical Society: Washington, D.C., 1984.
(3) Snyder, H. L.; Meakin, P.; Reich, S. *J. Chem. Phys., Part I* **1983**, *78* (6), 3334; *Macromolecules* **1983**, *16*, 757.
(4) Hashimoto, T., Kumaki, J.; Kawai, H. *Macromolecules* **1983**, *16*, 641.
(5) Hashimoto, T.; Itakura, M.; Hasegawa, H. *J. Chem. Phys.* **1986**, *85*, 6118.
(6) Herkt-Maetzky, C.; Schelten, J. *Phys. Rev. Lett.* **1983**, *51*, 896.
(7) Bates, F. S.; Wiltzius, P.; Heffiner, W. R. *Phys. Rev. Lett.* **1988**, *60*, 1538.
(8) Chan, J. W. *J. Chem. Phys.* **1977**, *66*, 3667.
(9) Siggia, E. D. *Phys. Rev. A* **1979**, *20*, 595.
(10) Ball, R. C.; Essery, R. L. H. *J. Phys.: Condens. Matter* **1990**, *2*, 10303.
(11) Wiltzius, P.; Cumming, A. *Phys. Rev. Lett.* **1991**, *66*, 3000.
(12) Guenoun, P.; Beysens, D.; Robert, M. *Phys. Rev. Lett.* **1990**, *65*, 2406.
(13) Jones, R. A. L.; Norton, L. J.; Kramer, E. J.; Bates, F. S.; Wiltzius, P. *Phys. Rev. Lett.* **1991**, *66*, 1326.
(14) Bruder, F.; Brenn, R. *Phys. Rev. Lett.* **1992**, *69*, 624.

(15) Tummala, R. R.; Ryamszewski, E. J. *Microelectronics Packaging Handbook*; Van Nostrand Reinhold: New York, 1989.
(16) Cotts, P. M.; Volksen, W. *Polym. News* **1990**, *15*, 106.
(17) Harris, F. W. In *Polyimides*; Wilson, D., Stenzenberger, H. D., Hergenrother, P. M., Eds.; Blackie & Sons: Glasgow, UK, **1990**, p 1.
(18) Chakravorty, K. K.; Cech, J. M.; Chien, C. P.; Lathrop, L. S.; Tanielian, M. H.; Young, P. L. *J. Electrochem. Soc.* **1990**, *137*, 961.
(19) Rubner, R.; Ahne, H.; Kuhn, E.; Kolodziej, G. *Photogr. Sci. Eng.* **1979**, *23*, 303.
(20) Wilson, D. In *Polyimides*; Wilson, D., Stenzenberger, H. D., Hergenrother, P. M., Eds.; Blackie & Sons: Glasgow, UK, **1990**; p 187.
(21) Hergenrother, P. In *Polyimides*; Wilson, D., Stenzenberger, H. D., Hergenrother, P. M., Eds.; Blackie & Sons: Glasgow, UK, **1990**, p 158.
(22) Brenker, M. J.; Feger, C. *J. Polym. Sci., Polym. Chem. Ed.* **1987**, *25*, 2005.
(23) Feger, C.; Saraf, R. F. *Advances in Polyimide Science and Technology*; Feger, C., Khojasteh, M. M., Htoo, M., Eds.; Technomic: Lancaster, PA, **1992**; p 141.
(24) Ginsberg, R.; Susko, J. R. In *Polyimides: Synthesis and Characterization*; Mittal, K., Ed.; Plenum: New York, **1984**; Vol. I, p 237.
(25) *Polymer Handbook*, 2nd ed.; Brandrup, J., Immergut, E. H., Eds.; J. Wiley and Sons, Inc.: New York, 1975.
(26) Saraf, R. F.; Ostrander, S.; Roldan, J. M., in preparation.
(27) Shi, B. H.; Harrison, C.; Cumming, A. *Phys. Rev. Lett.* **1993**, *70*, 206.
(28) Spiegel, M. R. *Mathematical Handbook of Tables and Formulas, Schaum's Outline Series*; McGraw-Hill: New York, 1968.